Review of Scientific Instruments

# Space-resolved visible spectroscopy for two-dimensional measurement of hydrogen and impurity emission spectra and of plasma flow in the edge stochastic layer of LHD

Cite as: Rev. Sci. Instrum. **88**, 033501 (2017); https://doi.org/10.1063/1.4976963
Submitted: 27 June 2016 • Accepted: 07 February 2017 • Published Online: 02 March 2017

M. Kobayashi, S. Morita and M. Goto

# Space-resolved visible spectroscopy for two-dimensional measurement of hydrogen and impurity emission spectra and of plasma flow in the edge stochastic layer of LHD

M. Kobayashi,[a] S. Morita, and M. Goto
*National Institute for Fusion Science, National Institutes of Natural Sciences, Oroshi-cho 322-6, Toki 509-5292, Japan and Department of Fusion Science, Graduate University for Advanced Studies, Oroshi-cho 322-6, Toki 509-5292, Japan*

(Received 27 June 2016; accepted 7 February 2017; published online 2 March 2017)

A space-resolved visible spectrometer system has been developed for two-dimensional (2D) distribution measurements of hydrogen and impurity emission spectra and of plasma flow in the edge stochastic layer of Large Helical Device (LHD). Astigmatism of the spectrometer has been suppressed by introducing additional toroidal and spherical mirrors. A good focal image at the exit slit is realized in a wide wavelength range (75 nm) as well as in a wide slit height direction (26 mm) with a 300 grooves/mm grating. The capability of the spectrometer optical system for the 2D measurement and further possible improvements are discussed in detail. An optical fiber array of 130 channels with a lens unit is used to spatially resolve the edge plasma into different magnetic field structure components: divertor strike points, divertor legs, X-point of the legs, the stochastic layer, and the last closed flux surface. With a 300 grooves/mm grating, the 2D distributions of several hydrogen and impurity line emissions are simultaneously obtained with absolute intensities. A clear correlation is obtained between the magnetic field structure and the emission intensity. With a 2400 grooves/mm grating with a good spectral resolution (0.03 nm/pixel), the 2D distributions of impurity flow velocity are obtained from the Doppler shift measurement. The wavelength position is accurately calibrated by investigating the wavelength dispersion as well as by correcting a mechanical error of the optical setting in the spectrometer. The uncertainty in the velocity is reduced to less than 10% of a typical impurity velocity $\sim 10^4$ m/s. A temporal change in the flow directions is observed at different spatial locations in divertor detachment plasma. *Published by AIP Publishing.* [http://dx.doi.org/10.1063/1.4976963]

## I. INTRODUCTION

Understanding of transport of fuel and impurity species in the edge region of magnetically confined fusion devices is one of the critical issues for the realization of a future reactor in terms of fueling efficiency, impurity screening, and control of edge radiation.[1] As a characteristic of the plasma transport, it exhibits a very fast transport along the magnetic field lines compared to the transport perpendicular to the field lines. Therefore, the transport of fuel and impurities is largely affected by the magnetic field structure. In tokamaks, edge impurity and hydrogen emissions have been investigated using spectroscopic systems,[2–5] where interesting plasma transport properties have been revealed. Helical devices, however, usually have a complex magnetic field structure due to the intrinsic non-axisymmetric configuration as compared to tokamaks, and we need special care to conduct the spectroscopic measurements.

In the Large Helical Device (LHD), there appears a stochastic layer in the edge region, which is induced by an overlap of different modes of the magnetic field spectrum produced by the helical coils.[6] The stochastic layer is connected to the divertor plates through divertor legs, which rotate in the poloidal direction while moving along the toroidal direction, according to the helicity of the helical coils. In order to study the plasma transport in this edge region, it is important to develop a space-resolved spectroscopic system, which encompasses the entire edge region in its viewing area, such as the stochastic layer, divertor legs, the divertor strike points on the target plates, and the last closed flux surface (LCFS). In LHD, there have been developed spectroscopic systems to provide a spatial distribution of impurity emissions in visible[7,8] as well as in EUV[9] and VUV[10] ranges. In most of the cases, however, the line of sight passes through both the edge and the confinement regions, and thus it has been difficult to resolve such magnetic field structures mentioned above.

In this paper, we describe a visible spectroscopic system, which has been recently developed to meet the requirements mentioned above in LHD. The system should provide a two-dimensional (2D) distribution of emission spectra from hydrogen and impurities over a sufficient coverage in space and with a good spatial resolution. For this purpose, the visible spectrometer has to sufficiently delete the astigmatism in the wider area on the output image because a large number of channels are necessary for a fiber array to observe the edge plasma as widely as possible. In addition, the spectrometer must fulfill both the high throughput and the high spectral resolution due to the relatively weak intensity of visible emissions from the divertor region and due to the Doppler shift measurement for the plasma flow determination. We have thus

[a]Author to whom correspondence should be addressed. Electronic mail: kobayashi.masahiro@lhd.nifs.ac.jp

adopted an astigmatism-corrected 30 cm Czerny-Turner-type spectrometer with three gratings. Since the spectrometer is equipped with computer-optimized toroidal spherical mirrors, which adjust the optical path length of each light, the astigmatism is expected to be corrected and deleted sufficiently over the entire output image of the fiber array. The short focal length of 30 cm can increase the spectrometer throughput. In addition, the choice of 300 and 2400 grooves/mm gratings brings us the high throughput and high spectral resolution modes, respectively. As a result, the present system makes possible the measurements of spatiotemporal evolution of 2D distributions of hydrogen and impurity emissions during detachment transition and radiation collapse in relation to each magnetic field structure component for the first time in LHD. An impurity motion velocity is also observed from Doppler shift measurements, and the 2D distributions of edge plasma flow, for example, a clear change in the flow directions at the different spatial locations and at the detachment transition, are successfully obtained. These results are extremely important information for understanding the edge plasma transport not only in the detached plasma but also in the stochastic magnetic field layer. The result is also very useful because it can be directly compared with numerical simulation to validate the existing transport model.[11–13]

In Sec. II, the basic specification and the viewing area of the system are described in relation to the magnetic field structure of LHD. In Section III, detailed results of the measurements and reconstructed 2D distribution of impurity and hydrogen emissions are presented. In Section IV, the estimation of impurity flow velocity and an absolute calibration of wavelength of the spectrometer are presented with 2D distribution of $C^{2+}$ velocity in the stochastic magnetic field layer. The paper is summarized in Section V.

## II. SPACE-RESOLVED VISIBLE SPECTROSCOPY WITH 2D FIBER ARRAY

### A. Spectrometer

The spectrometer is a Czerny-Turner-type spectrometer with a focal length of 30 cm (MK-300, BUNKOUKEIKI Co., Ltd.), which is optimized to suppress the astigmatism as much as possible by using a toroidal and an additional spherical mirror in the optical path, so that a clear vertical separation of the fiber image at the exit slit is realized. This enables us to use a full vertical extent of the exit slit over a wide wavelength range, and thus to use such a large number of fibers, which are fully resolved without cross talk between the adjacent channels. Specification of the spectrometer and the optical system is summarized in Table I. A schematic figure of the optical system of the spectrometer is shown in Fig. 1. The system consists of an entrance slit, one toroidal mirror, one plane mirror, three gratings on a rotatable table, two spherical mirrors, and a detector at the exit slit. The visible light from the entrance slit is collimated by the toroidal mirror, which has different radii of curvatures in the meridional (vertical) and sagittal (horizontal) planes, $r_v$ and $r_h$, respectively. This toroidal mirror is intended to correct the astigmatism caused by the finite angle, $\alpha$, of the incident rays with the mirror axis. After being reflected by the plane mirror, the light is diffracted by the gratings, which are mounted on a rotatable table. Three gratings are installed with the different groove densities, 300, 1800, and 2400 grooves/mm. Each grating has a reciprocal linear dispersion of 10.5, 1.3, and 1.1 nm/mm, respectively, as shown in Table I. The light after the diffraction is reflected by the two spherical mirrors (spherical mirror 1 and 2 in Fig. 1) and focused on to the detector at the exit slit. Here the additional spherical mirror (spherical mirror 1) has been introduced in order to correct astigmatism, as explained below.

The focal distances of the meridional (vertical) and sagittal (horizontal) images along the chief ray, measured from the mirror surface, are expressed as[14]

$$s_{vn} = \frac{r_{vn}\cos\alpha_n}{2}, \tag{1}$$

$$s_{hn} = \frac{r_{hn}}{2\cos\alpha_n}, \tag{2}$$

respectively. The subscripts $n$ denote the collimating (n = 1, in the present case, the toroidal mirror) and focusing (n = 2, spherical mirror 2) mirrors. The astigmatism is accumulated in collimating and focusing mirrors. Thus the amount of astigmatism (astigmatic difference), $\delta s$, is written as

$$\delta s = (s_{h1} - s_{v1}) + (s_{h2} - s_{v2}). \tag{3}$$

The astigmatism could be corrected by adjusting $r_v$ and $r_h$ properly to reduce $\delta s$ as much as possible.

After diffraction at the grating, however, each ray of a different wavelength has a different diffraction angle $\theta_d$ according to the grating equation

TABLE I. Specifications of the spectrometer MK-300 and fiber array.

| | |
|---|---|
| Focal length | 300 mm |
| F-number | 4.4 |
| Wavelength range | 200–1000 nm |
| Three gratings with different | 300 grooves/mm (blazed at 500 nm, dispersion = 10.5 nm/mm) |
| groove density (blazed | 1800 grooves/mm (blazed at 600 nm, dispersion = 1.3 nm/mm) |
| grating) | 2400 grooves/mm (blazed at 400 nm, dispersion = 1.1 nm/mm) |
| CCD detector size | 26.7 (vertical) × 6.7 (horizontal) mm, 16 bit |
| (DU-920P-BU2, ANDOR) | (1024 × 255 pixels, 26 × 26 $\mu$m/pixel) |
| Fiber core diameter | 50 $\mu$m (130 channels) |
| Lens magnification | 1200 at a location 4050 mm ahead |

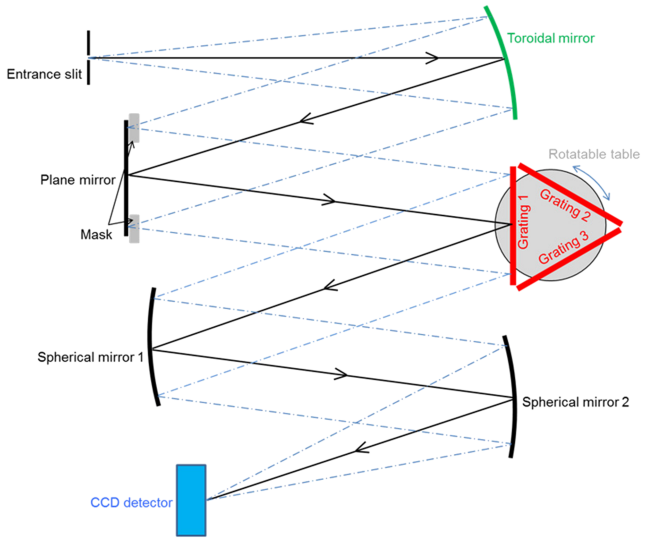


FIG. 1. Schematic of the optical system of the spectrometer. The system consists of an entrance slit, one toroidal mirror, one plane mirror, three gratings mounted on a rotatable table, two spherical mirrors, and a detector at the exit slit. The black solid lines represent the chief ray in the optical system. The mask on the plane mirror is used to correct coma.

$$\sin\theta_i + \sin\theta_d = m d \lambda, \tag{4}$$

where $\theta_i$, $\theta_d$, $m$, $d$, $\lambda$ represent, angles of incident and diffraction, diffraction order, groove density, and wavelength, respectively. This results in different incident angles to the focusing mirror depending on wavelength, $\alpha(\lambda)$. According to the Eqs. (1)–(3), this gives rise to a different astigmatism for a different wavelength. This is the reason for the distortion of the image distant from the central wavelength, that is, in the edge regions of the detector in the wavelength dispersion direction. This "wavelength dependent astigmatism" cannot be corrected by the toroidal mirror with radii of $r_v$ and $r_h$, which are effective only for the central wavelength.

An additional spherical mirror (spherical mirror 1 in Fig. 1) is introduced to correct the angle of each ray of a different wavelength, in such a way that the rays most distant from the axis of the mirror, i.e., at the outer most region of the optical path, are made parallel to the ray on the axis. In this way, the difference of the incident angle of each ray to the focusing mirror (spherical mirror 2) is minimized on average, and thus the astigmatism due to the wavelength difference can be minimized. In the present case, Eq. (3) can be written as

$$\delta s(\lambda) = \left(\frac{r_{h1}}{2\cos\alpha_1} - \frac{r_{v1}\cos\alpha_1}{2}\right) + \left(\frac{r_2}{2\cos\alpha_2} - \frac{r_2\cos\alpha_2}{2}\right), \tag{5}$$

where the subscripts 1 and 2 represent the toroidal mirror and the spherical mirror 2 in Fig. 1, respectively. The first and second terms represent the astigmatism difference at the toroidal mirror and spherical mirror 2, respectively. For spherical mirror 2, $r_{v2} = r_{h2} = r_2$. It is noted that $\alpha_2 \approx$ constant independent of the wavelength due to the correction by the spherical mirror 1 as explained above. Numerical calculation of ray tracing has been performed to minimize $\delta s$ as low as possible. Figure 2 shows the image at the detector after introducing the additional spherical mirror. It is clearly seen that a good separation of the

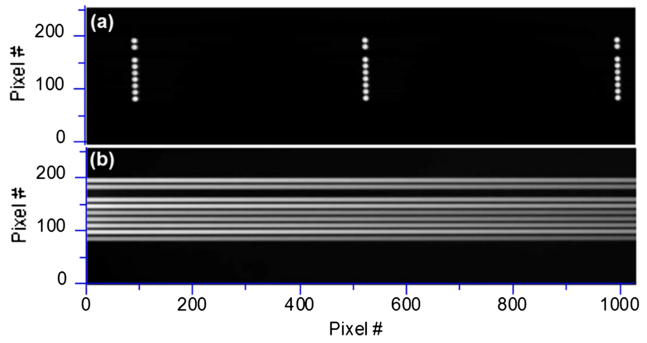


FIG. 2. CCD images of the spectrometer with correction of "wavelength-dependent" astigmatism with the additional toroidal and spherical mirrors. 9 optic fibers with core diameter of 250 $\mu$m are used. Slit width of 250 $\mu$m, exposure time of 0.3 s. (a) Hg I emission (546.074 nm). Three images are overlaid with different central wavelength settings of the spectrometer with 520, 546, and 570 nm, where each of them produces the right, central, and left images, respectively. (b) Halogen lamp with central wavelength of 546.074 nm.

images between channels is obtained in the entire wavelength range (in the horizontal direction), for both spectra of Hg lamp (Fig. 2(a)) and the continuous spectra of halogen lamp (Fig. 2(b)). The optical system then realizes the measurements with a large number of channels to provide a wide spatial coverage and good spatial resolution of line emission distributions.

A charge-coupled-device (CCD) detector (DU-920P-BU2, ANDOR Co., Ltd.) is used as a detector and placed at the exit slit position. The CCD has 1024 × 255 pixels with a pixel size of 26 × 26 $\mu$m, and the quantum efficiency is 50%-60% in a wavelength range of 250–800 nm. The dynamic range of the sensor is 16 bit and is cooled to −50 °C during operation. The read out speed is 3.0 MHz at maximum and the CCD is usually operated with an image transfer mode. After the data acquisition, the data are processed to obtain spectrum at each channel by binning.

### B. Fiber array and its focus on CCD detector

The fiber array made of quartz consists of 130 optical fibers with a core diameter of 50 $\mu$m (clad diameter of 62.5 $\mu$m). The smaller diameter of the fiber was selected to provide better spatial resolution, while ensuring enough light intensity in the measurements. The end surfaces of the 130 fibers are aligned vertically with 150 $\mu$m apart each other, that is, 100 $\mu$m interval between the edges of each fiber core, and are placed at the entrance slit of the spectrometer. In order to accommodate the large number of the fiber channels, the CCD was rotated by 90° from the original setting, such that the long axis side of the detector (1024 pixels) is in the vertical direction, while the short axis side is in the horizontal (wavelength) direction. Thus the wavelength range, which can be measured with the detector (short axis side, 255 pixels), becomes shorter than the original range, that is, ~75 and ~7 nm for 300 and 2400 grooves/mm, respectively, while the spectrometer system itself is capable of a range of 200–1000 nm. Figure 3 shows an obtained CCD image with the 130 channel fiber array for 546.07 nm line (7s–6p) of a mercury (Hg) lamp using the 300 grooves/mm grating. The 130 channels are numbered from bottom to top. The enlarged views at the channels 1 to 5, 63 to 67, and 126 to 130 are also shown on

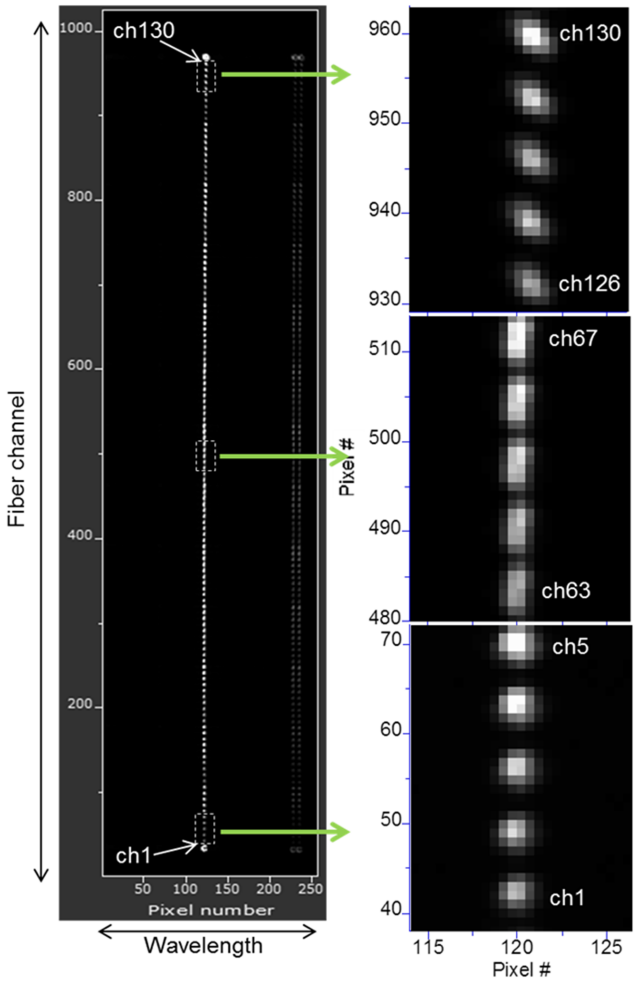


FIG. 3. A CCD image of fiber array (core diameter of 50 $\mu$m) taken with a 300 grooves/mm grating, an entrance slit width of 50 $\mu$m, an exposure time of 3 s for 546.07 nm line of an Hg lamp. The 130 channels are aligned vertically and numbered from bottom to top. The enlarged views of the images from ch1 to 5, ch63 to 67, and ch126 to 130 are shown on the right panels. At the top and bottom of the image, "reference fibers" (core diameter of 115 $\mu$m) are attached. These fibers are connected to a calibration lamp during the calibration of the wavelength and the LHD discharges. The images of these fibers are used to correct the possible deviation of the absolute wavelength between calibration phase and the LHD experiments caused by mechanical error of the spectrometer.

the right panels. It is seen that all the channels are well separated from each other in order to ensure the measurements with 130 fiber array. Here the vertical extent of the detector is 26.7 mm, as shown in Table I. At both ends of the aligned 130 fibers, i.e., top and bottom of the fiber image, "reference" fibers with core diameter of 115 $\mu$m are attached (see Fig. 3). These fibers are connected to a calibration lamp (Hg or noble gas) during both the wavelength calibration and the discharges in LHD. The image of these fibers is used to correct the possible deviation of the absolute wavelength between the calibration and the LHD experimental phases, which is caused by mechanical error when rotating the gratings, as described in Section IV.

At the CCD surface, the image is vertically magnified by a factor of 1.25 from that at the entrance slit due to the slit height magnification. This results in a vertical separation of each channel around seven pixels, while each peak is formed within six pixels in the vertical direction. It is seen in Fig. 3 that there is a gradient in the intensity along a set of 10 fibers. This is due to the comparable size of the calibration lamp and the lens unit attached to the other end of the fibers, where the fibers are structured to form 2D array in 10 columns × 13 rows, as shown below in Fig. 9(b). Therefore, all the fibers are not uniformly illuminated, resulting in the periodic intensity change at every 10 fibers as seen in the figure. Nevertheless, since each channel has a sufficient signal to noise ratio, we can evaluate a FWHM (full width at half maximum) at each channel. Shown in Fig. 4 with squares is a FWHM of the 546.07 nm line of Hg lamp with the 300 grooves/mm grating as a function of channels, obtained from the data of Fig. 3. The results show that the spectral line is well resolved for all the channels within ~3 pixels or less, where the FWHM tends to slightly increase for the upper and bottom region of the CCD, that is, for smaller and larger channels numbers.

All the channels are absolutely calibrated in intensity using the integrating sphere with a halogen lamp (Labsphere, Inc. Model# AS-01635-000 SC-5500). The same optics as the actual measurements are inserted into the integrating sphere to irradiate all the channels uniformly. Figure 5 shows a CCD image, where the fiber array is illuminated uniformly by the integrating sphere, with gating of 300 grooves/mm and central wavelength of 540 nm. A clear separation between the channels in a wide wavelength range (75 nm) is demonstrated. The resulting output signals from the CCD for all channels at 546 nm are shown in Fig. 4 with circles, where the intensity becomes smaller while moving to the edge of the CCD, i.e., at the smaller and larger channel numbers. Given an absolute spectral radiance of the integrating sphere, the absolute sensitivity of the system is calculated to provide a unit of $Wm^{-2}$ $sr^{-1}$ $nm^{-1}$ for the intensity. The obtained calibration factors are shown in Fig. 6 in a wavelength range of 350 to 700 nm for different channels. There is a systematic asymmetry of the calibration factor with respect to the central channel 65. One possible reason for the up-down asymmetry in the calibration factor is a slight vertical shift of the fiber array by 6 pixels lower than the center of the optical system. This means that the smaller channel numbers are more distant from the center compared to the larger channels. Another reason is a possible tilting of the fiber array with respect to the slit direction. Since the intensity calibration is performed with a slit size, which

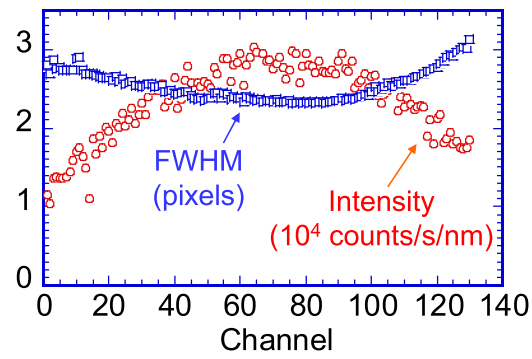


FIG. 4. Squares show full width at half maximum (FWHM) of the 546.07 nm line of an Hg lamp (squares) as a function of channel, obtained from the data of Fig. 3. Circles show the CCD signals at 546 nm when all the fibers are irradiated uniformly with integrating spheres with a tungsten lamp, obtained from the data of Fig. 5.

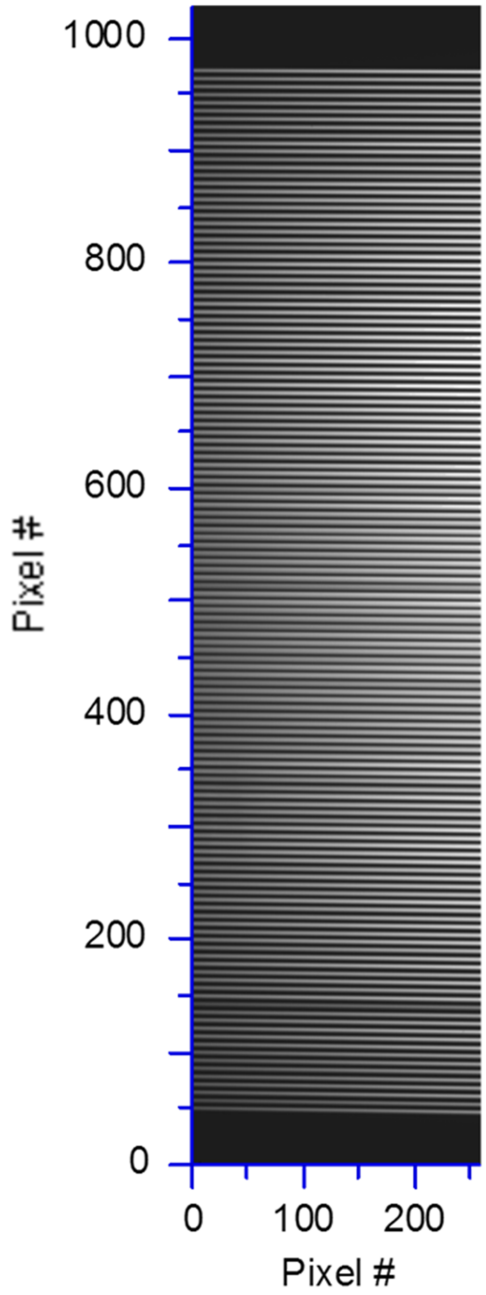


FIG. 5. A CCD image of the 130 fibers uniformly illuminated by an integrating sphere with a halogen lamp. A slit width of 50 $\mu$m, an exposure time of 5 s, the central wavelength of 540 nm, and a grating of 300 grooves/mm.

is comparable to the fiber core diameter, the small tilt of the fiber array to the slit direction leads to interference of the light by the slit. Since the spectrometer has no fine adjustor of the fiber array angle against the slit direction, it is rather difficult to realize precise alignment. This situation must be improved in a future upgrade of the present instrument. However, since the measurements during experiments have been carried out without changing the fiber alignment at the calibration phase, the validity of the estimation of absolute intensity is ensured.

### C. Correction of coma

By using the 2400 grooves/mm grating, which provides a better spectral resolution, one can analyze the Doppler shift of

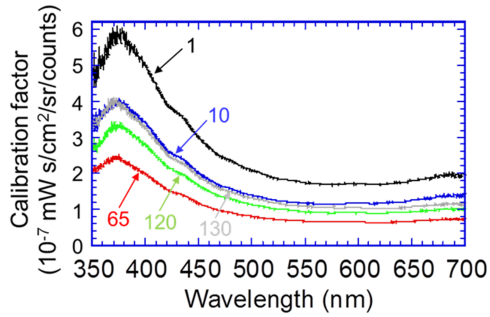


FIG. 6. Calibration factors obtained in the absolute calibration using the integrating sphere with a halogen lamp for wavelength range from 350 to 700 nm. The factors are plotted for the channels of 1, 10, 65, 120, and 130 as indicated by the numbers in the figure.

the spectrum caused by the plasma flow. At the initial phase in the present work, we found that the shape of the spectrum at the CCD detector is slightly deformed, as shown in Fig. 7 (dashed line with open circles for the original setting of mirror width = 43.5 mm), where a spectrum of 546.07 nm from an Hg lamp is shown with the 2400 grooves/mm grating and an entrance slit width of 20 $\mu$m. This is considered due to coma caused by off-axis light. In order to improve the spectrum shape, the optical path was limited by masking the edge region of a plane rectangular mirror placed in front of the

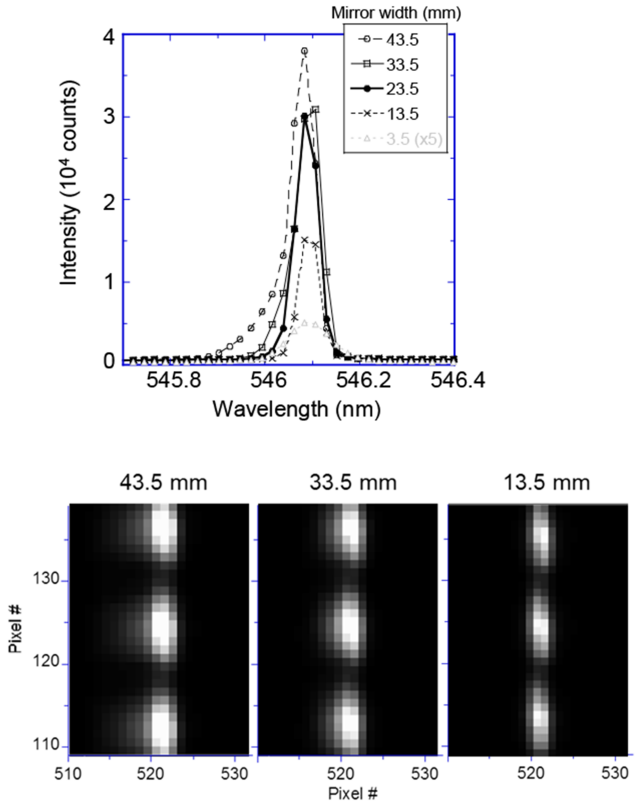


FIG. 7. Top panel: Shape of spectra of a line 546.07 nm from an Hg lamp taken with 2400 grooves/mm and an entrance slit width of 20 $\mu$m, for different mirror widths in front of the grating (optical path widths) in the spectrometer: 43.5 (open circles, original), 33.5 (open squares), 23.5 (closed circles), 13.5 (crosses), and 3.5 (open triangles, with intensity increased by a factor of 5) mm, respectively. Bottom panels: CCD images of the spectra around the central channel for the different mirror widths, 43.5, 33.5, and 13.5 mm, respectively.

grating, as shown in Fig. 1. The mirror size was originally 43.5 mm wide in a horizontal direction. For checking the spectrum shape, the width is gradually changed using the mask at both of the horizontal ends. Figure 7 shows the resulting spectrum shape and CCD images with different mirror widths (optical path widths). As the mirror width is reduced, the shape of the spectrum becomes more symmetric with respect to the center of the peak wavelength of 546.07 nm. At the same time, however, the intensity becomes weaker against the reduction of the width, as seen in Fig. 7(a). In order to maintain a good signal to noise ratio while achieving the symmetry of the spectrum as much as possible, the optimum mirror width was determined to be 21 mm.

### D. Field of view

Figure 8 shows a schematic view of the fiber array location in relation to the LHD vacuum vessel, magnetic field structure, and divertor plates. The optical fiber array is located at the outboard side of LHD, looking towards the upper part of the torus as shown in Fig. 8. In the figure, field lines of the divertor legs and the divertor plates are also shown. The field of view of the fiber array is shown in Fig. 9(a) together with the magnetic field lines of the divertor legs, the trajectory of X-points, an envelope of the LCFS, and the divertor plates. The connection length distribution in a poloidal cross section is plotted in Fig. 10, where the geometry of the edge magnetic field structure, such as the divertor legs, the stochastic layer, and the LCFS, is readily recognized. By comparing Fig. 9(a) with Fig. 10, one can relate the field line structure in the field of view to those in Fig. 10 as indicated in the figure. The field lines colored with red and yellow in Fig. 9(a) represent the divertor legs connected to the bottom and upper divertor plates shown in Fig. 10, respectively. The trajectory of the X-point, where the two groups of divertor legs (red and yellow) meet each other, is indicated in Fig. 9(a) with a white line. The trajectory rotates around the LCFS according to the helicity of the helical coils. It is noted that, in this field of view, the edge region is well decomposed to different components of the magnetic field structure, that is, the LCFS, the stochastic layer (the region between the LCFS and the X-point trajectory), the

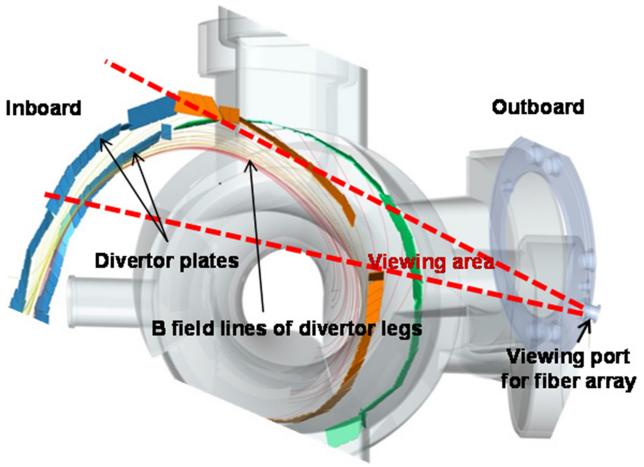


FIG. 8. Schematic of viewing area of the fiber array, the divertor plates, and the field lines of divertor legs. The fiber array is located at the viewing port at the outboard side.

divertor legs, and the divertor strike points. The view avoids an overlap of the lines of sight with those along the confinement region. Thus, the 2D distributions of hydrogen/impurity emission spectra in this viewing area can provide distinct information regarding the relation between the edge radiation and the magnetic field structure. It is also noted that the line of sight is almost tangential to the field lines, as seen in Fig. 8. Therefore, a velocity estimated from the Doppler shift of spectra almost reflects a component parallel to the field lines. The analysis of flow velocity is described in Section IV.

The 130 fibers are placed in a rectangle (10 × 13) shape at the viewing port of LHD in order to resolve the edge region in a 2D view. The field of view of the fiber array is focused on the edge region with a set of lenses, such that each fiber core has ~6 cm diameter at a location 4050 mm ahead of the fiber surface (a magnification of 1200), as shown in Fig. 9(b). The smaller diameter of the fiber was selected in order to provide better spatial resolution, while ensuring enough light intensity in the measurements. At the four corners of the 2D fiber image, "dummy" fibers (core diameter of 115 $\mu$m and clad diameter of 125 $\mu$m) are attached, which are used to adjust the viewing angle of the fiber array using laser light injected to the fibers.

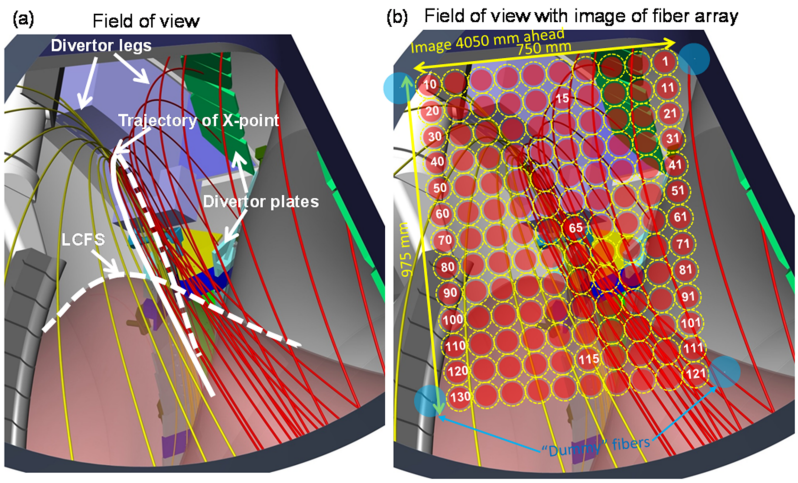


FIG. 9. (a) Field of view of the fiber array with magnetic field structure indicated. Correspondence between the field of view and the magnetic field structure in Fig. 10 is identified with the divertor legs, X-point trajectory, divertor plates, and the LCFS, as indicated in the figures. The red and yellow lines represent magnetic field lines of divertor legs connected to the bottom and upper divertor plates in Fig. 10. (b) Field of view with images of 130ch fiber array overlaid. Fiber core image is projected through the lens unit with a magnification of 1200 at a location 4050 mm ahead, where the image of each fiber core is 6 cm diameter. The numbers in each circle indicate channel numbers. At the four corners of the 2D fiber image, "dummy" fibers (blue circles, core diameter of 115 $\mu$m) are attached, which are used to adjust viewing location of the fiber array in the torus with laser beam injected in to the fibers.

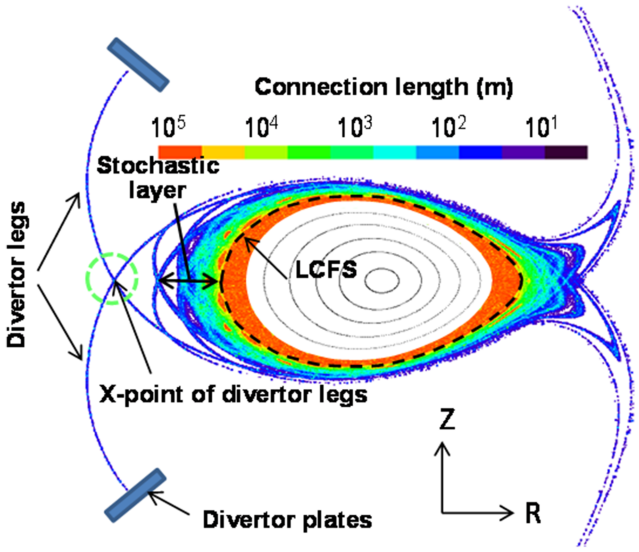


FIG. 10. Poloidal cross section of the connection length distribution. The magnetic field structure is indicated. Correspondence between the connection length distribution and the field of view in Fig. 9 is identified with the divertor legs, X-point trajectory, divertor plates, and the LCFS, as indicated in the figure.

## III. MEASUREMENT OF SPECTRA AND RECONSTRUCTION OF 2D DISTRIBUTIONS

Figure 11 shows time traces of plasma parameters (line averaged density, neutral bean (NB) injection power, radiated power, and divertor particle flux) of the shot #121787 with a magnetic configuration of $R_{ax}$ = 3.90 m (magnetic axis), Bt = 2.54 T. The density is gradually increased, while the divertor particle flux starts to decrease around t = 5.7 s in spite of the density ramp up, indicating a transition to detached phase. And then finally a radiation collapse sets in at t ~ 6.2 s. The spectra obtained with the wavelength range of 425–500 nm during this discharge are plotted in Fig. 12 for the three timings at t = 5.05, 6.10, and 6.25 s, as indicated in Fig. 11 with dashed vertical lines. The spectra are shown for the three channels, 15, 65, and 115, which correspond to divertor legs, stochastic layer or near

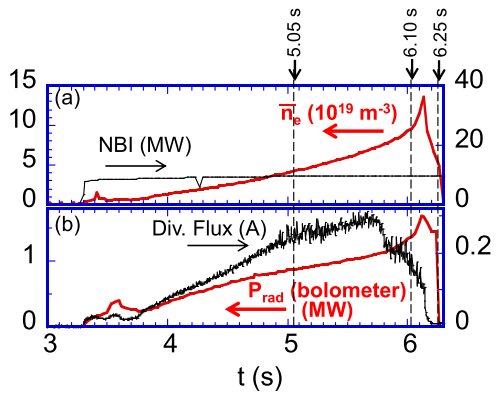


FIG. 11. Time traces of plasma parameters of the density ramp-up discharge, shot #121787 with a magnetic configuration of $R_{ax}$ = 3.90 m, Bt = 2.54 T. (a) Line averaged density (thick red line) and NB injection power (thin black line), (b) radiated power measured with bolometer (thick red line) and divertor particle flux (thin black line). The three timings at t = 5.05, 6.10, and 6.25 s are indicated with dashed vertical lines, at which timing the spectra are shown in Fig. 12.

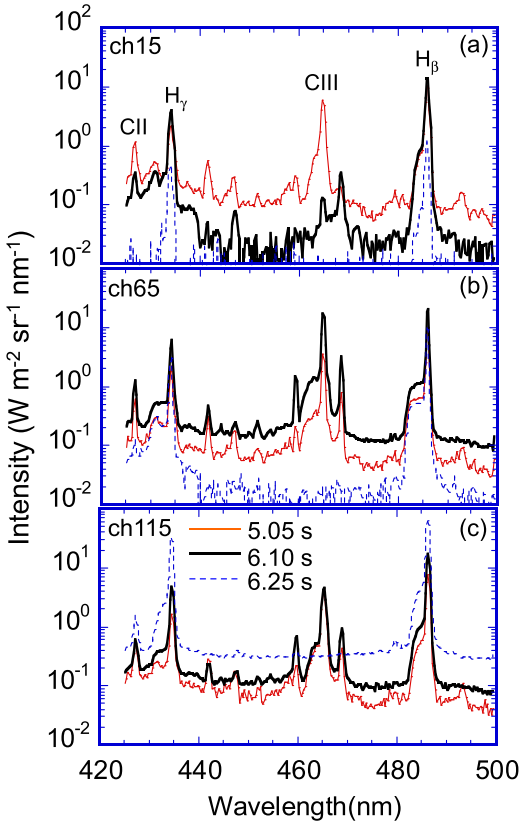


FIG. 12. Obtained spectra during the shot #121787 at the timings of t = 5.05 (thin red), 6.10 (thick black), and 6.25 (dashed) s, as indicated in Fig. 11. (a) ch15, (b) ch65, and (c) ch115. The spatial locations of the channels are indicated in Fig. 9(b). The data were taken with the 300 grooves/mm grating and an entrance slit width of 30 $\mu$m. The cycle time of the acquisition was set to 0.15 s (6.67 Hz) with the CCD exposure time of 8.39 ms for each frame. The vertical axis is in a logarithmic scale.

the X-point of divertor legs, and the region inside the LCFS, respectively, as indicated in Fig. 9(b). The data were taken with the 300 grooves/mm grating and an entrance slit width of 30 $\mu$m. The cycle time of the acquisition was set to 0.15 s (6.67 Hz) with the CCD exposure time of 8.39 ms for each frame. The vertical axis is in a logarithmic scale. It is seen that for each channel, we could obtain sufficient intensity for the typical emission lines such as $H_\beta$ (486.1 nm) and $H_\gamma$ (434.0 nm) from hydrogen, and CIII (464.7 nm, 3p-3s) and CII (426.7 nm, 4f-3d) from carbon originating from the divertor plates, etc. The good signal to noise ratio in spite of the relatively short exposure time and of the small fiber core diameter is attributed to the optical system of the present spectrometer with a focal length of 30 cm, which is optimized to enhance brightness.

It is seen from Fig. 12 that the temporal evolution of each line differs depending on the channels as well as on the spectral line. For example, the hydrogen line, $H_\beta$, tends to decrease with increasing density at the divertor leg (ch15), while it increases inside the LCFS (ch115), etc. An entire picture of the temporal evolution of the emission distribution is obtained by collecting the intensity of each line and reconstructing a 2D image, as shown in Fig. 13, where the distributions of CII and $H_\beta$ are plotted for the different time frames. At the attached phase of t = 5.05 s, the CII emission is distributed from the divertor plates towards the upstream region, as shown in Fig. 13(a).

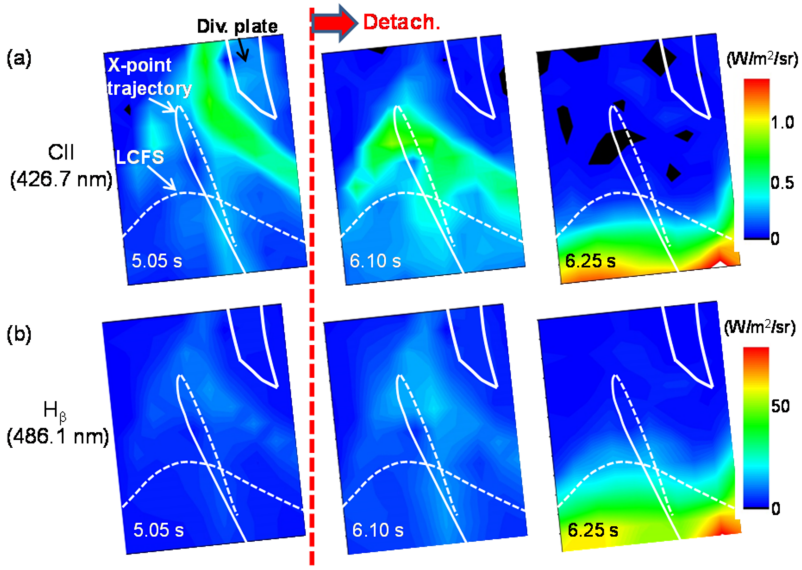


FIG. 13. 2D distributions of (a) CII and (b) $H_\beta$ emissions reconstructed from the spectra shown in Fig. 12. The locations of divertor plates, trajectory of X-point, and the LCFS are indicated in the figures.

The $H_\beta$ shows also a spatial pattern similar to the CII, as shown in Fig. 13(b). At t = 6.10 s, where the divertor particle flux is suppressed significantly after the roll over around t = 5.7 s, and the radiated power starts to increase rapidly toward the radiation collapse, it is clearly observed that the CII emission "detaches" from the divertor plate and moves toward the LCFS. At t = 6.25 s, where the discharge is terminated by the radiation collapse, the CII emission penetrates inside the LCFS. Regarding the $H_\beta$, similar behavior as those of CII is observed, while the clear "detachment" of the emission from the divertor plates is observed only at the last frame of t = 6.25 s. The results show a sufficient capability of the present system to provide a 2D distribution of various emissions from the edge plasma of LHD and to study the temporal evolution of the hydrogen and impurity in relation to the magnetic field structure.

## IV. IMPURITY FLOW VELOCITY MEASUREMENT FROM DOPPLER SHIFT ANALYSIS

### A. Absolute calibration of wavelength

In order to determine the absolute wavelength, we have first investigated a wavelength dispersion over a wide range of wavelength. Figure 14 shows the result of the dispersion, where various calibration lamps were used to provide reference emission lines. It is clearly seen that the wavelength dispersion gradually changes from 1.23 nm/mm at 300 nm down to 0.77 nm/mm at 600 nm. The dependence is fitted with a quadratic function such as,

$$\frac{d\lambda}{dx} = a_0 + a_1\lambda + a_2\lambda^2, \tag{6}$$

where $\lambda$ and $dx$ represent the wavelength and the linear dispersion at the exit slit, respectively. Here, we present an example of a Doppler shift analysis for CIII emission (464.742 nm). It is found that the two XeI emissions, 462.428 nm (7p-6s) and 467.123 nm (7p-6s), from the calibration lamp can be measured simultaneously together with CIII within the wavelength interval of 7 nm, which is the measurable wavelength range with the 2400 grooves/mm grating. Figure 15(a) shows the CCD image of XeI lines during a calibration phase for the 130 channel fibers. The channels are numbered from bottom to top. The two arrows provide absolute wavelength at $x = x_1$ and $x_2$ such that $\lambda(x_1) = \lambda_1 = 462.428$ and $\lambda(x_2) = \lambda_2 = 467.123$ nm for each channel. In-between $x_1$ and $x_2$, the wavelength is interpolated using the nonlinear dependence of Eq. (6) for each channel. It is seen that in Fig. 15(a), there is a horizontal position shift due to "grating smile," which is caused by a finite tilt angle of incident ray to the grating in vertical (groove) direction, when the ray comes from the off-axis region. The shift is inversely proportional to the reciprocal liner dispersion, $d\lambda/dx$. Therefore it is pronounced with the grating of 2400 grooves/mm, which has small $d\lambda/dx \sim 1.1$ nm/mm, and the shift is ~14.9 pixels. There exists the shift also in the Fig. 3 with grating of 300 grooves/mm, which has larger $d\lambda/dx \sim 10.5$ nm/mm. But the shift is so small, ~1.4 pixels, that it is not visible in the figure.

The reference fibers are illuminated with the XeI lines during both the calibration phase and the experimental phase,

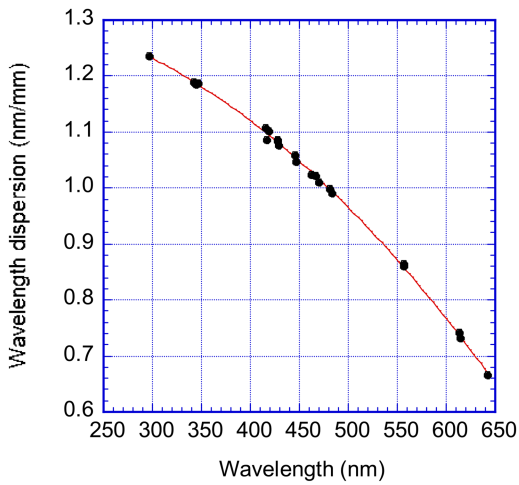


FIG. 14. Wavelength dispersion of the spectrometer, with the 2400 grooves/mm grating, obtained by using various calibration lamps, with a slit width of 50 $\mu$m. The data are fitted with a quadratic function, Equation (6).

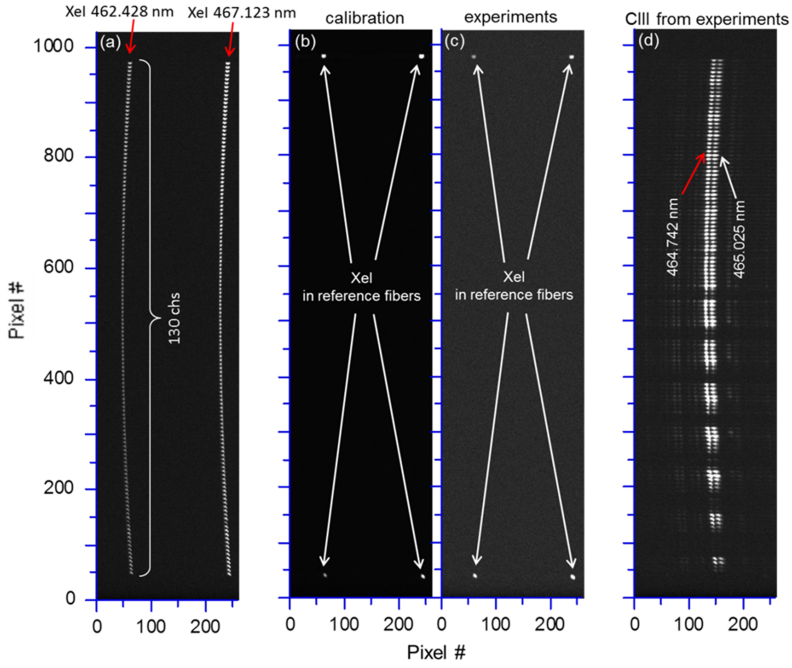


FIG. 15. CCD images of fibers with the 2400 grooves/mm grating and an entrance slit width of 50 $\mu$m. The 130 channels are numbered from bottom to top. (a) XeI lines (462.428 and 467.123 nm) from calibration lamp imaged with the 130 channel fibers, during calibration phase. (b) The XeI lines for "reference fibers" during the calibration phase. (c) The XeI lines for "reference fibers" during the experiment phase. (d) CIII emissions (464.742 and 465.025 nm) from the plasma in LHD imaged with the 130 channel fibers during the experiments.

as shown in Figs. 15(b) and 15(c), in order to correct the wavelength deviation between the two phases, which arises due to the mechanical error during the grating rotation. Typically, the error is within a few pixels. Figure 15(d) shows an example of CIII emission measured during experiments, where a slight wavelength shift brought by the Doppler effect can be identified, in addition to the systematic horizontal shift due to the astigmatism.

The accuracy of the Doppler shift analysis is estimated from the XeI lines, where the spectral profile is fitted with a Gaussian distribution, and the errors of the peak location, $\delta\lambda$, are converted to an error in the velocity, such as $\delta V = c\frac{\delta\lambda}{\lambda}$ with $c$ being the speed of light. The results are plotted in Fig. 16, where it is clearly seen that the error becomes large at smaller and larger channel numbers, that is, away from the midplane of CCD, which is due to the deformation of the focal image as moving towards the edge of the CCD. Figure 17 shows the enlarged CCD images at channels 1-5, 62-68, and 126-130 of that in Fig. 15(a). As seen in the figures, the images at the top and bottom regions of the CCD detector (i.e., channels of 1-5 and 126-130) are strongly deformed, while they are still well separated from each other between the channels. It is also noted that the deformation is not up-down symmetric. In the bottom region (channels of 1-5), the shape of the images is elongated vertically and inclined with respect to the horizontal direction, while in the top region (channels of 126-130), they are elongated in the horizontal direction with slight bending. These deformations are considered to occur by the combination of several aberrations arising in this off-axis region, (i.e., far outside of the paraxial region), such as coma, grating smile, possible residual astigmatism, curvature of field, and distortion.[10] Although the optical system has been optimized to reduce the astigmatism as much as possible, complete suppression of all these aberrations is impossible in a realistic system. The up-down asymmetry of the deformation is possibly due to slight misalignment of the optical system, which consists of several spherical and toroidal mirrors together with the gratings on the rotating table, and the CCD detector. There may be also errors in the shape of the mirror surface. Any small misalignment could be enhanced to affect the resulting images at the exit slit in the far off-axis region. Nevertheless, it should be noted that the images of different channels are reasonably separated from each other even at the very top and the very bottom edges of the CCD as shown in the figure. The separation thus enables us to process the data separately between channels.

Figures 17(d), 17(e), and 17(f) show the spectra of channel 1, 65, and 130 after binning, where the lines show the Gaussian fit. It is found that the spectral width becomes large in the channels of 1 and 130 compared to 65, which is due to the deformation of the image as described above. But the spectra are still reasonably fitted with a Gaussian function as shown

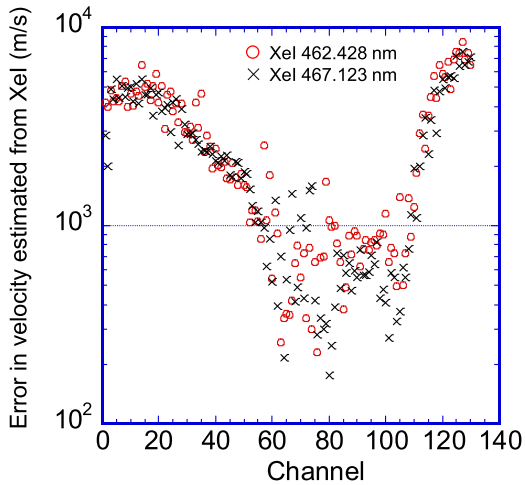


FIG. 16. Errors in velocity evaluation from the Doppler shift analysis, estimated from the error of peak location of XeI lines in Fig. 15 (slit width of 50 $\mu$m) with Gaussian fit, $\Delta\lambda$, such as $\Delta V = c\frac{\Delta\lambda}{\lambda}$ (c is the speed of light). Circles and crosses are for XeI lines of 462.428 and 467.123 nm, respectively.

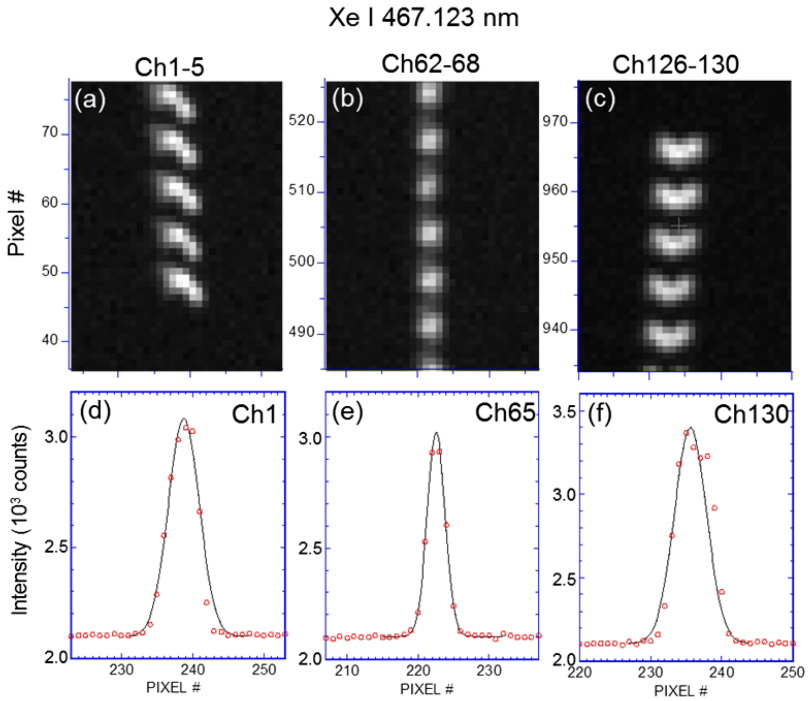


FIG. 17. (a)–(c) The enlarged CCD images of the Xe I (467.123 nm) line with the grating of 2400 grooves/mm for the channels of 1-5, 62-68, and 126-130, respectively. The same data set as Fig. 15(a), 15(d)–15(f) spectra obtained after binning for channels of 1, 65, and 130, respectively. The lines show Gaussian fits.

in the figure. Due to the broadening of the spectra at the off-axis region, the error of the peak location, $\Delta\lambda$, in the channel 1 and 130 becomes large as shown in Fig. 16. It is also found that in the channel of 130 there is slight splitting of the spectrum, which is caused by the deformation as shown in Fig. 17(c). This leads to the larger error in channel 130 than that in channel 1. This kind of up-down asymmetry of the aberrations could be the reason why the error grows more rapidly in channels 110-130 than in channels 1-20, as seen in Fig. 16.

As will be shown below, the typical values of the velocity estimated from CIII are in an order of $10^4$ m/s. Therefore, the velocity estimated from the central channels has reasonably good accuracy with an error less than 10%, while for the channels away from the center, the error reach up to ~50%.

### B. Application to LHD discharges

The time traces of plasma parameters in LHD shot# 128200 are plotted in Fig. 18, where the resonant magnetic perturbation (RMP) is applied and the density is gradually increased. The discharge goes to the detachment around t = 5.9 s as shown by the decrease in the divertor particle flux with a concomitant increase of the radiated power. The detachment phase is sustained until the end of the discharge due to the application of RMP. The spectral data were taken with a sampling rate of 6.67 Hz (cycle time of 0.15 s) and an exposure time of 41.34 ms for each frame. The obtained spectra around CIII (464.742 nm) are plotted in Fig. 19 at a time frame of t = 5.52 s, just before the detachment transition, for channels #44 to #47. The channels correspond to the horizontal scan across the X-point of divertor legs as shown in Figs. 9(a) and 9(b). It is clearly seen that the spectra show a wavelength shift in shorter or longer sides, depending on the channels. The peak position obtained by Gaussian fit ($\lambda'$) is compared to the original peak position ($\lambda_0$), and the Doppler velocity is computed using the formula

$$V = c\frac{(\lambda_0/\lambda')^2 - 1}{1 + (\lambda_0/\lambda')^2}. \quad (7)$$

The temporal evolution of the velocity computed with the Doppler effect is plotted in Fig. 20 for the channels #44 to #47. The positive and negative values represent the directions toward and away from the point of view (the fiber array), respectively. It is found that the velocity is in an order of $10^4$ m/s, as mentioned above. Since the viewing direction is almost tangential to the field lines, the velocity is considered to represent a parallel velocity along the magnetic field. If we assume typical values of $T_e \sim T_i \sim 10$ eV along the divertor legs in LHD,[15,16] the obtained velocity corresponds to 40%–50% of

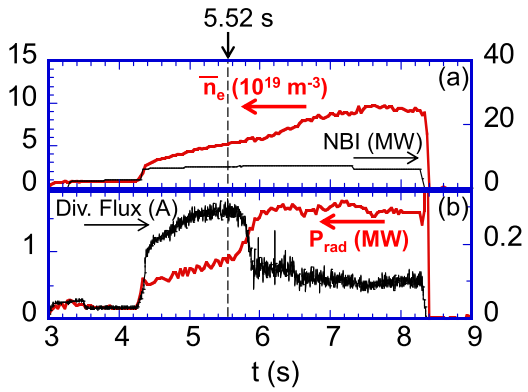


FIG. 18. Time traces of (a) line averaged density (thick red line) and NB injection power (thin black line), (b) radiated power measured with bolometer (thick red line) and divertor particle flux (thin black line) in #128200, $R_{ax}$ = 3.90 m, Bt = 2.54 T, with RMP application. The discharge goes to detachment phase at around t = 5.9 s. The dashed vertical line indicates the timing of t = 5.52 s, at which Figs. 19 and 21 are analyzed.

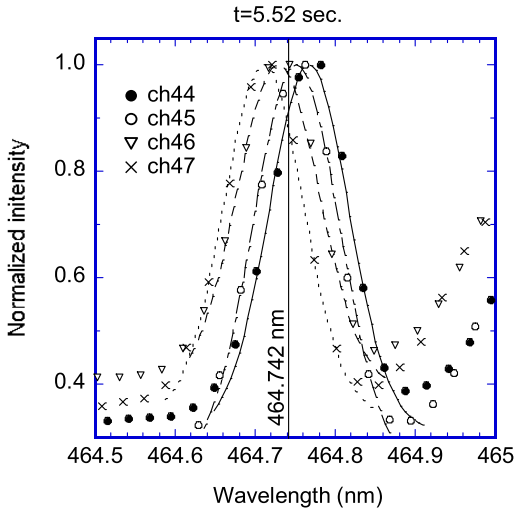


FIG. 19. Spectra obtained at t = 5.52 s in the shot #128200 (Fig. 18) for channels of 44 (closed circles), 45 (open circles), 46 (triangles), and 47 (crosses). The lines represent Gaussian fit for each channel. The vertical line indicates the original wavelength of CIII. The channels correspond to horizontal scan across the X-point of divertor legs as shown in Fig. 9. The data were taken with the 2400 grooves/mm grating, an entrance slit width of 50 $\mu$m, a sampling rate of 6.67 Hz (cycle time of 0.15 s), and an exposure time of 41.34 ms.

the sound speed of background plasma. After the increase in NB injection power at t ~ 4.3 s, the velocity becomes large and there appears a clear alternation of the flow direction depending on the channels. After the detachment transition at t = 5.9 s, the radiated power and the divertor flux become constant. The density, however, continues to increase up to t = 7 s. This means that the plasma is still not yet in a steady state until t = 7 s. This is a typical behavior of the detachment transition with RMP application. It might be related to a plasma response to the external RMP field. It is also found that the change of the flow speed occurs in a rather long time scale after the detachment transition until the flow direction becomes positive for all the channels at t = 6.3 s. They then remain nearly constant up to the end of discharge. The 2D distribution of the flow field is plotted in Fig. 21 for t = 5.52 s, where the red and blue colors indicate the positive and negative velocity as defined above. It is interestingly found that the flow alternation occurs almost

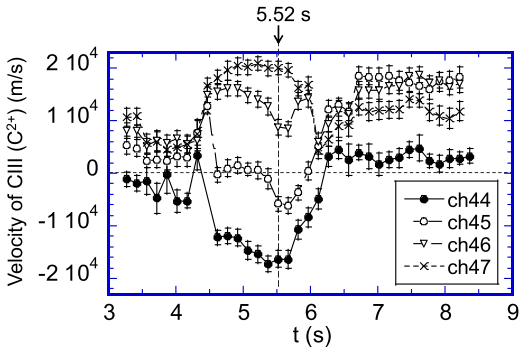


FIG. 20. Temporal evolutions of flow velocity of CIII ($C^{2+}$ ions) estimated from the Doppler shift analysis as shown in Fig. 19 (slit width of 50 $\mu$m), for channels of 44 (closed circles), 45 (open circles), 46 (triangles), and 47 (crosses). The data are for the shot #128200, as shown in Fig. 18. The positive and negative values represent the directions toward and away from the fiber array, respectively. The vertical dashed line indicates the timing of t = 5.52 s, at which Figs. 19 and 21 are analyzed.

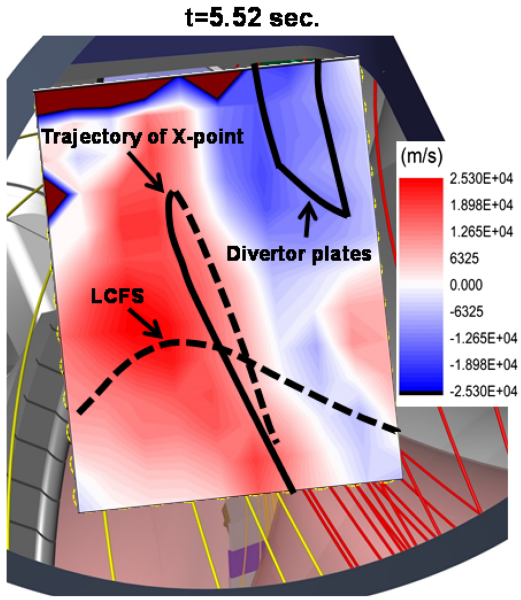


FIG. 21. 2D distribution of flow velocity of CIII ($C^{2+}$) estimated from the Doppler shift analysis, at t = 5.52 s of shot #128200, slit width of 50 $\mu$m. Red and blue colors represent the positive and negative directions of the flow, as defined in Fig. 20 and in the text. The trajectory of X-point of divertor legs and the envelope of LCFS are indicated with the solid lines.

with respect to the X-point trajectory of the divertor legs. This is considered to be reasonable since the divertor legs on the left hand side of the X-point are connected to the divertor plate in a positive direction as defined in the velocity, while the divertor legs on the right hand side are connected in a negative direction. Carbon impurity flow distribution has also been investigated in ASDEX Upgrade divertor II[2] and in DIII-D,[3] where the similar velocity speed (~$10^4$ m/s) was observed, as well as a flow reversal in the detachment plasma. Comparison of the flow distributions between tokamaks and stellarators will be an interesting work to understand the transport properties in the scrape-off layer.

The results indicate that the $C^{2+}$ ions flow toward divertor plates along the divertor legs at this timing. These analyses show that the present system can well determine the flow velocity of impurity ions using the Doppler shift analysis and provide a 2D distribution of the flow field in relation to the magnetic field structure.

## V. SUMMARY

The space-resolved visible spectroscopic system for measurements of 2D distributions of hydrogen and impurity emissions spectra has been developed in LHD. The astigmatism corrected spectrometer with 30 cm focal length is adopted to meet the following two requirements: One is to accommodate a large number of fibers for a wide spatial coverage of the field of view as well as for a good spatial resolution in the edge plasma region. Another one is to realize high throughput and high spectral resolution in order to obtain a good signal to noise ratio for the divertor radiation and for the Doppler shift measurements, respectively. An optical fiber array of 130 channels with 50 $\mu$m core diameter and a lens unit is installed on the outboard port of LHD such that the entire edge region

of the stochastic layer can be resolved into different magnetic field structure components, such as the divertor strike points, the divertor legs, the X-point of divertor legs, the stochastic layer, the LCFS, and the confinement region. The viewing area is free from an overlap with the emission in the confinement region.

The astigmatism of the spectrometer has been suppressed in wide wavelength range and in slit direction by introducing additional toroidal and spherical mirrors. The schemes of the aberration corrections and resulting CCD images are presented in detail. Capability of the optical system to resolve the large number of channels and possible improvements in future upgrade are discussed. It is shown that the current system enables a good spectral resolution and high throughput over the whole fiber channels. Thereby, the requirements for the present measurement system as mentioned above are satisfied, and the correlation between hydrogen/impurity emission distributions and the magnetic field structure can be studied. The data are important for understanding the edge plasma transport as well as to validate existing transport models through comparison with numerical simulations.

Using a 300 grooves/mm grating, spectra of the representative emission lines from the hydrogen and impurity of carbon, for example, $H_\alpha$, $H_\beta$, CII, CIII, and others, can be measured simultaneously. The 2D distributions of the emissions were reconstructed by picking up each line and by binning the CCD images at each channel. A clear correlation between the magnetic field structure and the emission is confirmed during the density ramp-up discharge of LHD, that is, "detachment" of the emission from the divertor plates and upstream shift at the detachment transition, and further penetration into the confinement region at a radiation collapse.

With good spectral resolution using a 2400 grooves/mm grating, the Doppler shift of impurity emission lines has been analyzed. The shape of the spectrum has been sufficiently improved from its original condition by correcting coma in the spectrometer, while maintaining enough signal to noise ratio. The absolute wavelength calibration was conducted by investigating the linear dispersion and by introducing "reference fibers" to define the reference emission from a calibration lamp. For example, two XeI lines are used for the analysis of CIII. The mechanical error of the optical system setting of the spectrometer was corrected by using the reference emissions, which are available for both the calibration and the experiment phases. An error in the Doppler shift estimation can be reduced to less than 10% of the typical velocity of the impurity of $\sim 10^4$ m/s for the 40 channels around the midplane of the CCD. Spatiotemporal evolution of parallel flow velocity of CIII ($C^{2+}$) has been obtained. A clear change in the flow speed and its direction has been observed for different spatial locations as a function of time in the discharge with detachment transition.

## ACKNOWLEDGMENTS

The authors are grateful to Mr. Akihito Nakamura, Mr. Takafumi Ikedo of Bunkoukeiki Co. Ltd., and Mr. Ken Matsuda of ANDOR Co. Ltd., for the technical support for the spectrometer. The authors are also grateful to Mitsubishi Cable Industries Ltd. for the technical support for the optical fibers during the development of the system. The authors wish to thank Professor B. J. Peterson and Dr. R. Sano for the fruitful discussions. The excellent works of the LHD experiment group for creating plasma discharges are greatly acknowledged. This work was financially supported by the NIFS budget ULPP026, and by Japan Society for the Promotion of Science Grant Nos. 25420893, 15H04236, and 16H04622.

[1] A. Loarte *et al.*, Nucl. Fusion **47**, S203 (2007).
[2] J. Gafert *et al.*, J. Nucl. Mater. **266-269**, 365 (1999).
[3] R. C. Isler *et al.*, Phys. Plasmas **6**, 541 (1999).
[4] M. B. Chowdhuri *et al.*, Nucl. Fusion **53**, 023006 (2013).
[5] T. Nakano *et al.*, J. Nucl. Mater. **390-391**, 255 (2009).
[6] N. Ohyabu *et al.*, Nucl. Fusion **34**, 387 (1994).
[7] M. Goto and S. Morita, Phys. Rev. E **65**, 026401 (2002).
[8] M. Goto and S. Morita, Rev. Sci. Instrum. **77**, 10F124 (2006).
[9] E. Wang, S. Morita, M. Goto, and C. Dong, Rev. Sci. Instrum. **83**, 043503 (2012).
[10] S. Morita and M. Goto, Rev. Sci. Instrum. **74**, 2036 (2003).
[11] M. Kobayashi, S. Morita *et al.*, Nucl. Fusion **53**, 033011 (2013).
[12] S. Dai *et al.*, Nucl. Fusion **56**, 066005 (2016).
[13] A. Bader *et al.*, Plasma Phys. Controlled Fusion **58**, 124006 (2016).
[14] G. S. Monk, *Light: Principles and Experiments*, 2nd ed. (Dover Publications, Inc., 1963).
[15] S. Masuzaki *et al.*, Nucl. Fusion **42**, 750 (2002).
[16] M. Kobayashi *et al.*, Fusion Sci. Technol. **58**, 220 (2010).